Shear banding and the isotropic-to-nematic transition in wormlike micelles

Elmar Fischer and Paul T. Callaghan
Institute of Fundamental Sciences–Physics, Massey University, Palmerston North, New Zealand
(Received 26 February 2001; published 12 June 2001)

Using deuterium NMR spectroscopy in a Couette cell, we observe shear-induced nematic ordering in the concentrated wormlike-micelle system CTAB/D_2O, and our results are qualitatively consistent with birefringence studies, and in exact quantitative agreement with the degree of order measured in neutron-diffraction measurements. The width of the nematic region depends on shear rate, as well as on the temperature proximity to the equilibrium isotropic-nematic transition. Comparison of the nematic order profiles with velocity profiles obtained under identical conditions shows quite clearly that the nematic state is not identifiable with a highly sheared, low viscosity layer, and we conclude that the process of shearing induces a nematic state of high viscosity, possibly associated with mesoscale ordering. We present a simple model in which transition from the high shear branch to the viscous nematic branch is counterbalanced by subsequent relaxation of nematic order.

DOI: 10.1103/PhysRevE.64.011501 PACS number(s): 83.10.−y, 83.50.Ax, 82.70.Uv, 68.18.Jk

INTRODUCTION

The phenomenon of shear banding in complex fluids has been the subject of intensive theoretical and experimental investigation in recent years. An early focus [1] was the ''spurt effect'' seen in the shear flow of polymer melts, and nicely explained by the tube model for entangled random coil polymers [2,3]. In that microscopic model, alignment of the chains leads to a reduction in viscosity with increasing shear rate, the phenomenon known as shear thinning. At higher shear, a critical rate is reached (on the order of the tube disengagement rate), beyond which the stress declines. This behavior, which is believed to be associated with strong chain alignment, results in flow that is inherently unstable. Such declining stress cannot, however, continue indefinitely, and eventually a rising stress, high shear branch may be expected to emerge [3], as shown schematically in Fig. 1. The existence of such a branch allows the fluid to phase-separate into regions of widely differing shear rate, under a common coexistence stress [4]. These regions will be associated with the intersections of a stress tie line with the upper and lower branches of the underlying flow curve and the proportions of each band will be as required to satisfy the average shear rate, $\dot{\gamma}$, namely

$$\dot{\gamma} = \phi_1 \dot{\gamma}_1 + \phi_2 \dot{\gamma}_2 , \tag{1}$$

where ϕ_1 and ϕ_2 are the respective volume fractions of the low shear rate ($\dot{\gamma}_1$) and high shear rate ($\dot{\gamma}_2$) phases [5]. The separation of the fluid into these states is commonly referred to as shear banding and the existence of a shear plateau in cone-and-plate measurements of the flow curve has been interpreted as an indication of underlying shear-banded flow [5].

The most dramatic evidence for banding effects has been found in the class of surfactant systems known as wormlike micelles [6–8]. These ''living polymers'' are formed by the self-assembly of certain amphiphilic molecules into long cylindrical structures whose flexibility and size are governed by the surfactant volume fraction, the salt concentration, and the temperature. The behavior of flexible wormlike micelles under shear is believed to resemble that of highly entangled random coil polymers [9,10]. In the semidilute region (up to a surfactant concentration, ϕ, of around 10%), the micelles overlap and form an entangled network. Reptation of the micelle chains is believed to play an important part in stress relaxation. However, unlike polymers, the micelles may continuously break and reform, and this breakage-recombination process [11] provides a second relaxation mechanism, a factor that is of considerable importance in understanding the rheology of these materials.

At higher concentrations ($\phi > 10\%$), steric interactions may cause the micellar threads to spontaneously orient. Most wormlike micelle systems exhibit an ordered nematic phase at sufficiently high concentration [12–14]. As a consequence, the flow behavior of these more concentrated systems may be governed by shear-induced phase transitions [12]. Even if the equilibrium state of the micellar fluid is isotropic, the proximity of an isotropic-to-nematic transition results in order-parameter fluctuations [15–19], and these may couple with the shear to drive the system into the nematic state [20–23]. The phenomenon of shear-induced isotropic-to-nematic (I-N) transitions has been invoked by several authors to explain shear-banding effects in wormlike micelle solutions [12,24–27].

Thus there are two distinct depictions of heterogeneous flow in wormlike micelles. One concerns a flow instability of

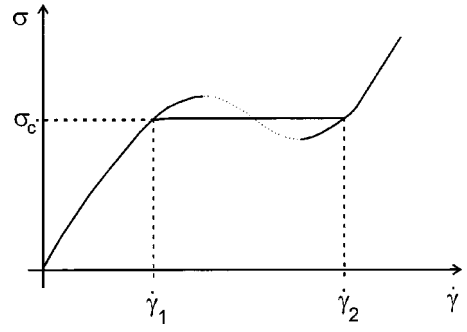

FIG. 1. Schematic flow curve for a material exhibiting a constitutive instability. At a fixed stress, two widely differing shear rates may coexist.

the micellar constitutive relation, governed by Doi-Edwards dynamics [2,3] in competition with breakage recombination. This picture is due to Cates and co-workers [28–30] and might be expected to apply to semidilute micellar systems distant from the equilibrium *I-N* transition. In the second approach, shearing the isotropic fluid in the vicinity of a nearby equilibrium *I-N* transition is believed to trigger a nonequilibrium phase transition to a nematic state and the coexistence of isotropic and nematic fluids of widely differing viscosities [12,24,31–34]. Both pictures have been invoked to explain shear-banding effects.

Just as there exists a dichotomy in the explanation of shear banding, so there exists a dual perspective in the direct observation of these phenomena. In the earliest experiments by Decruppe and co-workers [35,36] and Berret and coworkers [37,38], cylindrical Couette cells were used to deform wormlike micelle solutions while polarized light was passed through the annular gap along the vorticity direction. These measurements indicated the formation of distinct bands of differing birefringence, the width of these bands being governed by the average shear rate. Birefringence arises from anisotropy in the material refractive index so that a strong birefringence indicates an ordered phase. Two classes of fluids have been investigated. The first concerns concentrated micellar systems in which an *I-N* transition was proximate [12,14,25,27,35] while the second concerns semidilute micellar solutions in which an *I-N* transition was distant [34,38–40]. Examples of the first class include cetyltrimethylammonium bromide (CTAB)/water and cetylpyridinium chloride(CpyCl)/hexanol/brine. The second class includes CTAB/KBr/water and cetylpyridinium chloride/sodium salicylate (CpyCl/NaSal) systems both with and without added NaCl. In experiments carried out on systems close to an *I-N* transition, the existence of a shear-induced nematic phase has been strongly supported by neutron-diffraction measurements [25,27], whereas in the latter fluids, flow birefringence banding was observed but small-angle neutron-scattering measurements were inconclusive. In all these studies, the authors have associated the strongly birefringent phase with a high shear rate/low viscosity state and have routinely referred to the birefringence bands as ''shear bands.''

In an entirely different approach, Callaghan and coworkers have used nuclear magnetic resonance velocimetry to investigate the velocity profiles exhibited by wormlike micelle solutions in a wide range of geometries, including cone-and-plate flow, pipe flow, and Couette flow [41–45]. In most of these studies, the cetylpyridiniumchloride/sodium salicylate (CpyCl/NaSal) system has been studied far from an *I-N* transition. These NMR imaging experiments have clearly shown the existence of shear banding, and have revealed that these bands are typically narrow in width and can migrate within the flow field. Most importantly, these measurements reveal that the highest shear-rate state does not necessarily arise at the point of highest stress within the cell.

Recently, we have turned our attention to the CTAB/water system extensively studied via birefringence and neutron scattering [14,25]. This new work [46] combined two different NMR measurements in one system. In the first, we measured the velocity profile across the gap, locating both the high-shear-rate and low-shear-rate phases. In the second, we used deuterium NMR spectroscopy to measure the orientational ordering of the micelles, thus locating the nematic and isotropic phases. A remarkable outcome of this study was that there exists no simple correspondence between these physical states, in particular that the highly ordered phase does not exhibit high shear. In other words, a birefringence band is not, as first thought, a shear band, and the behavior of wormlike micelles, in the vicinity of an *I-N* transition, must be considerably more complex than previously believed.

In this paper, we report an extensive combined NMR velocimetry/NMR spectroscopy study with the wormlike micellar fluid, CTAB in D_2O, the system investigated in detail by Cappelaere *et al.* [25] using both flow birefringence and neutron scattering. We show the effect of both shear rate and temperature on the distribution of shear and molecular ordering in this system and we propose a model for shear-induced nonequilibrium *I-N* transitions in which competition between ordering and relaxation effects plays a crucial role. In particular, we will argue that a steady-state banded structure does not exist and that the observations made by NMR, by birefringence, and by neutron scattering represent well-defined time averages of continually varying structures.

THEORETICAL MODELS OF SHEAR BANDED FLOW

A. Constitutive instability in wormlike micelles

The existence of a constitutive flow instability for entangled polymers under shear flow is inherent to the Doi-Edwards model. The fact that the critical shear rate for the onset of these effects is on the order of the tube disengagement rate, τ_{rep}^{-1}, means, however, that polydispersity in the molar mass, M, can strongly damp the onset of spurt since $\tau_{\mathrm{rep}} \sim M^3$. In the case of flexible wormlike micelles, such polydispersity effects can be masked so that classical Doi-Edwards instability may be enhanced.

In the reptation-reaction model of Cates [11,47] for wormlike micelles, stress relaxation occurs via an interplay of reptation and breaking processes, the intrinsic relaxation times for these two processes being given by τ_{rep} and τ_{break}, respectively. In the fast breaking regime applicable in a wide class of wormlike surfactant solutions, i.e., when $\tau_{\mathrm{break}} \ll \tau_{\mathrm{rep}}$, the model predicts that at low frequencies, stress relaxation will be single exponential and the characteristic stress relaxation time will be given by

$$\tau_R = (\tau_{\mathrm{break}} \tau_{\mathrm{rep}})^{1/2}. \tag{2}$$

Because the breakage and recombination process provides preaveraging at a microscopic level, the time τ_R is independent of chain length polydispersity, and at low frequencies it represents a near-Maxwell behavior involving a single dominant relaxation time. At higher frequencies, the behavior is expected to be non-Maxwellian, and instead characterized by a spectrum of relaxation times.

The nonlinear viscosity of wormlike micelles can be explained by adapting the tube model to allow for the effect of

chain breakage and recombination [11,29]. This analysis suggests that the critical stress and corresponding critical shear rate (see Fig. 1) are given by

$$\sigma_c = \tfrac{2}{3} G_0 \quad \text{and} \quad \dot{\gamma}_c = 2.6/\tau_R , \tag{3}$$

where G_0 is the plateau modulus. At shear rates much greater than $\dot{\gamma}_c$, other dynamical processes will counteract the falling stress and a rising branch emerges. This branch may be due to the Rouse modes of the micelle transverse to the tube axis [5], local motion of the micelles, or the intrinsic viscosity of the solvent. The stress upturn at high shear rates generates the characteristic inflections in the flow curve shown in Fig. 1. This double-valuedness of the stress versus shear rate constitutive relationship in wormlike micelles leads to predictions of ''shear banding.'' The precise mechanism for stress selection in these coexistence states is uncertain and may depend in a subtle manner on shear history. One simplistic approach is to generate the tie line using a Maxwell equal-area construction, in analogy with the first-order phase transition in a liquid-gas system.

In wormlike micelle systems where the breakage/recombination time τ_R is sufficiently long, a simple Maxwellian behavior may no longer be observed. Such multiexponential relaxation, characteristic of semiflexible rodlike polymers, is often found in the absence of surface-charge-screening salt where electrostatic interactions between the surfactant molecules add to the steric constraints. The CTAB/water system used in the work presented here is apparently [25] of this type and the origins of any constitutive flow instability may lie in the classical Doi-Edwards description rather than in the reptation-reaction model.

B. Shear-induced isotropic-to-nematic transition

In the critical liquid-gas (LG) behavior of simple liquids, shear flow can cause the critical point to be shifted in temperature [15]. It is a remarkable feature of complex fluids that deformational flows can significantly modify phase transitions. One of the earliest observations of this effect was in the influence of shear flow on the demixing transition in high molecular weight polymer solutions [48]. More recently, birefringence measurements in wormlike micelle systems have suggested a shift in the *I-N* transition temperature.

The standard explanation for such shifts is based on a coupling of the stress with fluctuations in the order parameter near the phase transition [16,49], although in many systems, additional effects may enhance or compete. Shear flow has the effect of advecting and thereby suppressing fluctuations with characteristic times slower than $\dot{\gamma}^{-1}$. In a simple liquid near the liquid-gas transition, these slow modes tend to be the longer-wavelength fluctuations characteristic of critical behavior. Consequently, the suppression of these fluctuations tends to cause the critical point to be shifted to lower temperatures [15], although perturbation of the intermolecular Van der Waals interactions by the shear deformation counteracts this effect [23]. By contrast, in polymer demixing, stress enhances critical fluctuations and raises the demixing temperature [16,49]. In lyotropic liquid crystals exhibiting a first-order isotropic to lamellar (I-L) phase transition, nonlinear fluctuations in thermal equilibrium lower the *I-L* transition temperature. When a lyotropic liquid crystal experiences shear, the suppression of fluctuations is strongly anisotropic, those forming with layers normal to the flow being more severely affected. Because these more suppressed fluctuations are those that tend to frustrate equilibrium ordering, the *I-L* transition temperature is shifted to higher temperatures [19].

In nematogenic (e.g., rodlike) molecules, which exhibit an equilibrium nematic phase, deformational flow has the extra effect of inducing order directly. A detailed theoretical treatment of the *I-N* transition under shear flow has been given by Olmsted and Goldbart [23]. For nematogens, shear flow has three principal effects. It induces alignment and thus selects a specific orientation for ordering. The inherently biaxial nature of shear makes the *I-N* transition nonsymmetry breaking, thus influencing the critical point behavior. Finally, the flow suppresses fluctuations that frustrate ordering, thus causing the transition temperature to rise with increasing shear rate.

The theory of flow curve instability in nematic systems has been developed by Olmsted and co-workers [23,31–33,50–52]. A theory of rigid rod suspensions in shear flow has been given by Olmsted and Lu [31] using a modified Doi model in which free-energy terms that penalize spatial inhomogeneities and that represent the free energy of mixing are introduced. Thus the nematogen concentration is a variable in the Olmsted and Lu model. In this model, coexistence is associated with an inhomogeneous state spanning separate branches of the homogeneous flow curves, the coexistence state being determined by equating the chemical potential in the two phases. Inherent to this model is the assumption that the nematic phase has lower viscosity than the isotropic phase and thus comprises the high-shear-rate branch. Olmsted and co-workers have also identified stress-strain rate curves in which both strain rate and stress coexistence are possible, thus raising issues concerning the geometric character of the interfaces separating the differing phases.

It should be noted that the wormlike micelle systems under study in the present work are considerably more complex than rigid rods and that there exists no detailed microphysical theory pertaining to their nonequilibrium phase behavior. We shall present evidence here that, in these systems, the shear-induced nematic state does not simply comprise the high-shear-rate branch of the underlying flow curves, but instead may have a highly viscous character.

MEASUREMENT OF ORDERING USING DEUTERIUM NMR SPECTROSCOPY

The measurement of polymer deformation by optical methods relies on some underlying assumptions, for example the identity of the macroscopic and microscopic polarizability tensor, and the dominance of intrinsic birefringence over form birefringence. In our NMR method, the orientation of bond vectors is determined through nuclear spin interactions. We use nuclear magnetic resonance to determine the strength of the electric quadrupole interaction of deuterons, a quantity that depends in a very simple manner upon the relative ori-

entation of the electric-field gradient axis (the bond axis) and the polarizing magnetic field used to produce the nuclear Zeeman effect. In our experiments reported here, the deuteron is present in the water solvent. The small water molecules rapidly diffuse throughout the solution and thus sample the mean alignment of the host micelles. Because of the use of such an indirect probe, the measurement of alignment is not absolute, and, like the birefringence method, relies on an equivalent to the stress-optical coefficient.

A spin-one deuterium nucleus experiences an electric-quadrupole interaction between the nuclear quadrupole moment and the surrounding electric-field gradient. Because this interaction is experienced in the presence of a much larger Zeeman interaction between the magnetic-dipole moment and the polarizing magnetic field B_0, it is observed as a first-order perturbation projected along the spin quantization axis defined by the static magnetic field. For an axially symmetric electric-field gradient, as is typically found in an oxygen-deuterium bond of the water molecule, the quadrupole interaction takes the form [53,54]

$$H_Q=\frac{3eV_{zz}Q}{4I(2I-1)}P_2(\cos\theta)(3I_z^2-I^2). \tag{4}$$

Here θ is the angle between the field gradient axis and the polarizing magnetic field whose direction is labeled by z. V_{zz} is the electric-field gradient strength, Q is the nuclear quadrupole moment, and I is the nuclear spin quantum number. The effect of H_Q is to split the deuterium resonance into a doublet separated in frequency by $(\frac{3}{2}eV_{zz}Q/h)P_2(\cos\theta)$. The quadrupole interaction strength $\frac{3}{2}eV_{zz}Q/h$ is usually on the order of 100 kHz in partially ordered systems.

In simple isotropic liquids, molecular tumbling causes θ and hence H_Q to fluctuate. Provided that this motion is more rapid than the quadrupolar interaction strength, a condition that is true for all but the most viscous liquids, the quadrupolar Hamiltonian is averaged to zero. By contrast, in anisotropic liquids, the motional averaging is incomplete. In our case, the deuterated water molecule probes the nematic order experienced by the host micellar system. The rapidly diffusing and tumbling probe molecule will undergo steric interactions with micellar segments and experience an anisotropic mean orientation over the characteristic averaging time associated with the inverse quadrupolar splitting frequency [55]. This time is sufficiently long to produce a motional average over a length scale of tens of microns, and thus it represents a true ensemble mean. Thus the Legendre polynomial factor in Eq. (3) is averaged to

$$\overline{P_2(\cos\theta)}=S_{\mathrm{av}}P_2(\cos\alpha), \tag{5}$$

where α is the angle between the host director and the magnetic field, and S_{av} defines a local probe order parameter, a number that may be exceedingly small, and around 10^{-4}. The deuteron probe will thus exhibit a scaled-down quadrupole splitting given by

$$\Delta\nu=\left(\frac{3}{2}\frac{eV_{zz}Q}{h}\right)S_{\mathrm{av}}P_2(\cos\alpha). \tag{6}$$

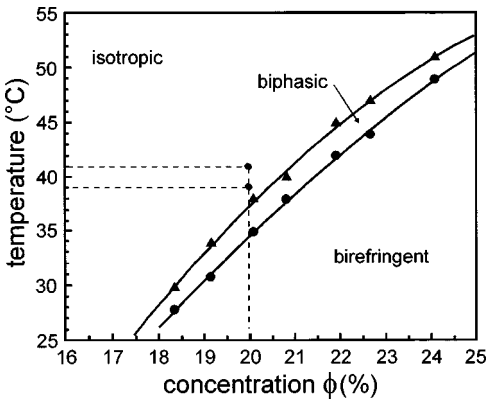

FIG. 2. Phase diagram for CTAB/D_2O taken from Ref. [25]. The vertical dashed line represents the concentration line at which NMR experiments were performed, in the temperature range from 39 to 41 °C.

While S_{av} will depend on surfactant concentration, its precise value is unimportant in the present analysis. The existence of a split doublet or a single peak will indicate the presence of nematic order or an isotropic state, respectively, in the host surfactant.

EXPERIMENT

We have carried out NMR and rheology measurements using aqueous salt-free solutions of CTAB in D_2O, as studied using flow birefringence and neutron scattering by Cappelaere *et al.* [25]. This solution is non-Maxwellian and exhibits a disperse spectrum of relaxation times, as found for a polydisperse system of unbreakable chains. Nonetheless, a distinct plateau in the flow curve is found, consistent with the coexistence of states with widely differing shear rate. We have chosen to study this system because of the clearly nematic character of the fluid under shear, both as indicated in the birefringence and neutron-scattering work of Cappelaere, and in our own nuclear-magnetic-resonance investigations.

CTAB was obtained from Acros Organics and dissolved in deuterated water (more than 99.92 at. % deuterium) from Apollo Scientific Ltd. Solutions were prepared by dissolving the surfactant and maintaining the solution in a sealed glass container at 45 °C for a period of 48 h. All experiments reported here were made on fresh samples prepared in this way, except where explicitly stated. The phase diagram [25] for CTAB-D_2O is shown in Fig. 2. We have chosen to work with a surfactant concentration $\phi=20\%$ and have carried out a series of experiments at temperatures both above and below the *I-N* transition. Note that the CTAB in D_2O concentration used in the NMR work is slightly higher than the value of $\phi=18\%$ of the birefringence and neutron-scattering study. We chose this higher concentration because of better-defined NMR spectroscopic features. However, we have worked at temperatures displaced from the *I-N* transition at $\phi=18\%$, similar to those used by Cappelaere *et al.* Further, we note that the flow curves obtained at $\phi=18\%$ and 20% are very similar. Thus we believe that our NMR data are directly comparable with the birefringence and neutron-scattering study.

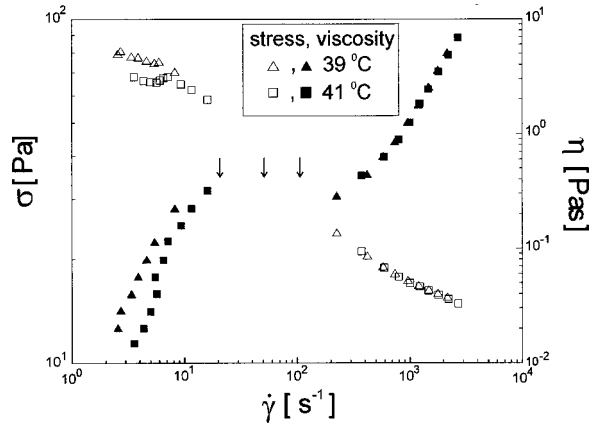

FIG. 3. Flow curves for 20% w/v CTAB/D_2O at temperatures of 39 and 41 °C in which a stress plateau is observed. The arrows indicate the shear rates at which NMR experiments have been performed.

The nonlinear rheology was studied using a Rheometrics RS-5000 working in the controlled stress mode. A cone and plate geometry was chosen with a diameter of the cone of 40 mm and a gap angle of 0.0391 rad. On a logarithmic scale, different stress values (ten points per decade) are selected between 10 and 100 Pa and the control unit of the rheometer tries to find a rotation rate of the cone compatible with the selected stress. For each stress value, a time of 300 s was given until the shear rate compatible with that stress value was measured. In order to avoid evaporation of the sample, a solvent trap has been used. For each temperature, a fresh sample from the storage container kept at 45 °C was used. Representative flow curves at 41 and 39 °C are shown in Fig. 3 and agree well with those found by Cappelaere *et al.* on similar solutions [25]. Below 10 s^{-1}, the solution is Newtonian while between 20 and 300 s^{-1} a distinct plateau is observed between lower and upper shear rates. This plateau is similar at both temperatures and represents a constant stress of around 35 Pa. Above 400 s^{-1}, a rising branch of stress is found with the behavior again close to Newtonian.

NMR velocimetry [54] and spectroscopy experiments were carried out on a Bruker AMX300 NMR spectrometer with microimaging capability, using the deuteron NMR signal at 45 MHz. Shear deformation was carried out using a specially constructed Couette cell made of PEEK, in which the ratio of the outer cylinder radius (19 mm) to the inner cylinder radius (17 mm) is 1.11, similar to that used in the birefringence cell of Cappelaere *et al.* A scale diagram of the cell is shown in Fig. 4(a). The cell inner cylinder is rotated by a drive shaft that sits in the bore of the magnet and is turned by a stepper-motor gearbox assembly mounted above the magnet bore [56]. Temperature control is via an airflow system in which sample temperatures are maintained to within 0.5 °C. Note that the average shear rate within the gap is determined by dividing the inner wall velocity by the gap width. Because this width is 1.00 mm, the shear rate in s^{-1} and the inner wall velocity in mm s^{-1} have the same numerical values.

Details of our NMR microscopy and velocimetry methods have been given elsewhere [54,56]. Figure 4(b) shows an

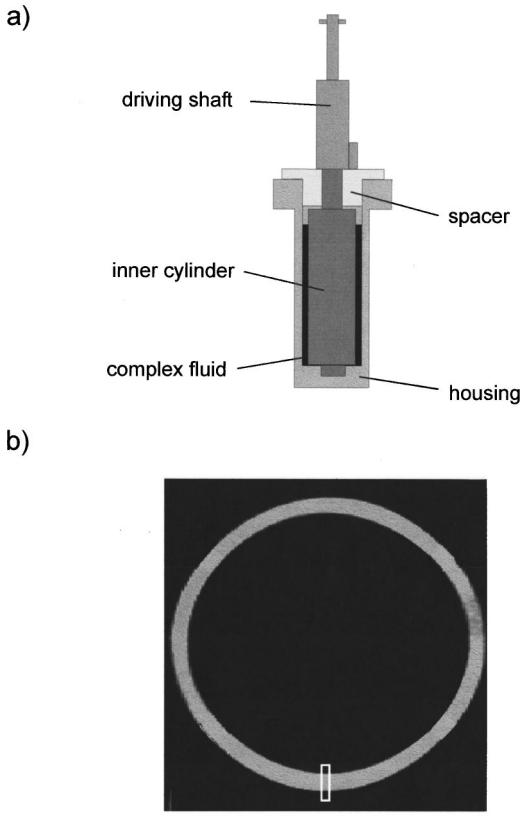

FIG. 4. (a) Scale diagram of Couette shearing cell used in this work. The OD and ID of the inner and outer cylinders, respectively, are 17 and 19 mm, giving an annular gap of 1 mm. (b) NMR micrograph of the fluid in the annulus of the Couette cell. The field of view is 20 mm and the white rectangle shows the region used to profile the gap.

NMR micrograph of the fluid in the annular gap, along with the region selected for velocity and spectroscopy profiling. The pulse sequence used for velocimetry is shown in Fig. 5(a) and incorporates two position-encoding magnetic-field gradient pulses of duration δ and amplitude g, in the successive dephasing and rephasing periods of a preceding spin echo. Displacement of fluid elements by a distance Z over the time Δ between the pulses results in a phase shift, $\exp(iqZ)$, in the corresponding pixel of the image where q is the wave vector associated with the field gradient pulse, and is given by $\gamma\delta g$, γ being the nuclear gyromagnetic ratio. By increasing the amplitude of the gradient pulses in eight successive steps, the signal in each pixel becomes ''wave-vector encoded.'' We are thus able to obtain a spectrum of the displacements. In particular, by inverse Fourier transformation of the signal in each pixel with respect to the gradient amplitude, we obtain the displacement distribution over the total acquisition time of around 1 h.

Figure 5(b) shows a different pulse sequence in which the image signal is encoded for the deuteron quadrupole interation. As in the velocimetry case, a spin echo is used to refocus unwanted magnetic (Zeeman) interactions. Because the quadrupolar interaction is bilinear in the spin operators [see Eq. (4)], this term in the spin Hamiltonian is unperturbed by the 180° rf refocusing pulse and thus the effect of the qua-

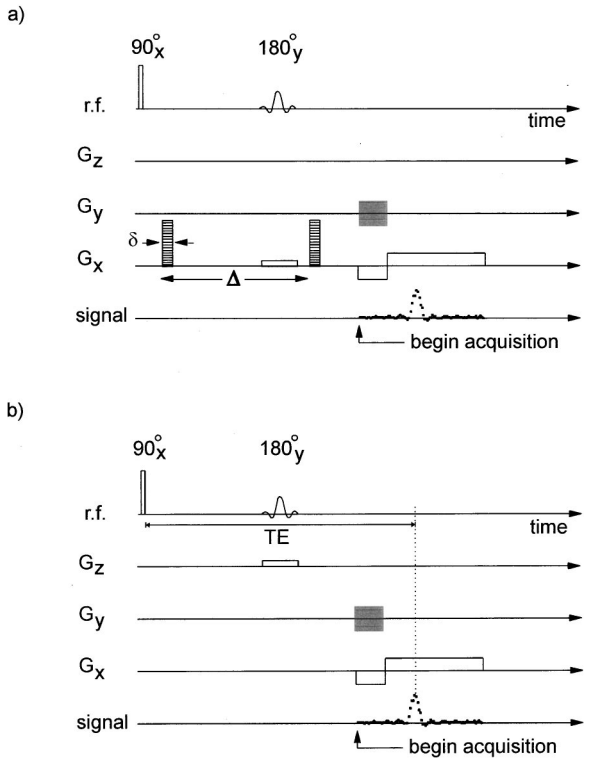

FIG. 5. Schematic rf and gradient pulse sequences for (a) velocity imaging and (b) spectroscopic imaging. The *x* and *y* directions correspond to the transverse plane of the cylinder. In (a), velocity encoding is along the *y* axis. Two narrow gradient (*q*) pulses of duration δ and separation Δ are increased in amplitude through eight separate values in successive image acquisitions. (b) The echo time TE is stepped in 32 successive values, to produce a phase encoding of the image that arises from the evolution of the spin system under the quadrupole interaction.

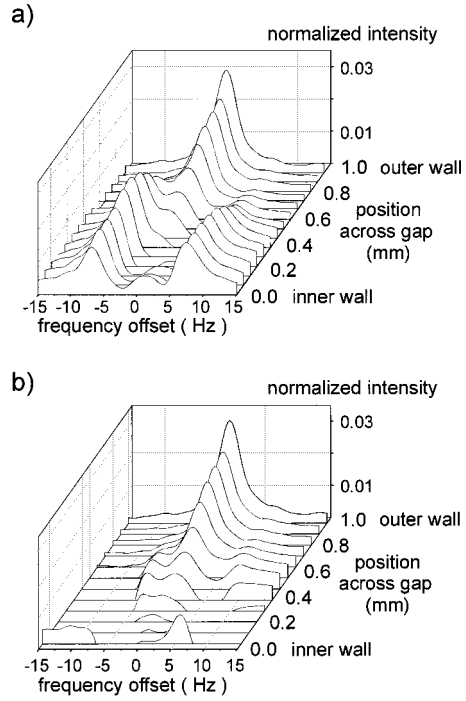

FIG. 6. Spatially resolved deuterium NMR spectra obtained using the pulse sequence of Fig. 5(b), for a 20% w/v CTAB/D_2O sample under a mean shear rate of 104 s^{-1} and at a temperature of 39 °C. The central peak arises from the isotropic phase while the doublet arises from the nematic phase. Note that the effect of the bipolar read gradient (G_x) is to cause a phase shift of the spectrum that depends upon the local velocity. Thus each spectrum shown has a characteristic phase that may be used to deduce the local velocity. In fact, this phase is different for the isotropic and nematic phases because of a difference in the mean velocity of each. In (a), the local phase is corrected in the data processing, so as to reveal a mostly absorption spectrum. In (b), the phase is absolute with respect to the outer wall and the spectral phase shifts reveal the effect of motion.

drupolar interaction remains. This quadrupole interaction imparts a frequency encoding, $\exp(i\Delta v\mathrm{TE})$, to the corresponding pixel of the image. Again, inverse Fourier transformation with respect to the echo time (TE) results in a deuteron NMR spectrum at each pixel. Thus we are able to image the deuterium NMR spectrum across the annular gap of the Couette cell.

RESULTS

A. Identification of the isotropic and nematic states

The previous study by Cappelaere *et al.* indicated the formation of a bright band of high birefringence at shear rates in excess of 20 s^{-1}, while neutron-scattering experiments exhibit a distinctly anisotropic scattering [25]. The remaining dark band in the optical work, while labeled isotropic, nonetheless exhibits a small birefringence from which an extinction angle may be calculated. The way in which we determine the relative proportions of the phases is shown in Fig. 6, where we display a series of deuteron NMR spectra at 80-μm intervals across the 1.0-mm gap. The shear rate is 105 s^{-1} and the temperature is 39 °C, approximately 3° above the onset of the equilibrium *I-N* transition. At the outer wall of the cell, where the stress is at a minimum, a single peak is found characteristic of an isotropic phase. At the inner wall, the spectrum is clearly split into a doublet of around 15-Hz separation, although the existence of a weak isotropic peak at the inner wall is also apparent. We shall refer to the singlet peak at 0 Hz as the isotropic peak and the doublet with 15-Hz splitting as the nematic peak. In all the work reported here, this nematic doublet has an identical splitting.

NMR spectra are acquired as both in-phase and quadrature phase signals from the heterodyne receiver. Thus they comprise complex numbers of arbitrary absolute phase. This phase may be subsequently adjusted by multiplying the entire spectrum by $\exp(i\phi)$, where ϕ may be varied until a pure absorption spectrum is displayed. In the spectra shown in Fig. 6(a), it was necessary to use a different value of ϕ for each position across the gap in order to optimize the overall absorption character of each spectrum. By contrast, in Fig. 6(b), where an identical phase correction is made at all positions, the spectral distortion is obvious. The reason for the variation in spectral phase across the gap can be seen by inspection of the pulse sequence shown in Fig. 5(b). The

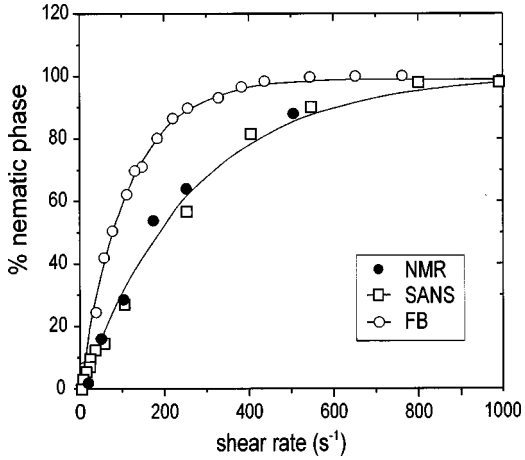

FIG. 7. The percentage of a nematic phase across the entire annulus, as a function of gap shear rate, as measured by birefringence (open circles), by small-angle neutron scattering (open squares) and by deuterium NMR (solid circles), for a 20% w/v CTAB/D_2O sample 3 C from the *I-N* transition. The birefringence and neutron-scattering data are from Ref. [25]. The agreement between NMR and small-angle neutron scattering is very good.

bipolar G_a gradient that is used to encode for position has the added effect of introducing a phase shift arising from flow parallel to the gap. The extent of that phase shift gives a measure of the average velocity at each position. As a consequence, the measurement of these phase shifts can be used to give an independent, albeit less accurate, measure of the velocity field experienced by the solution, to complement the more accurate Fourier velocimetry method based on the pulse sequence of Fig. 5(a).

The great advantage of the phase-shift method is that we are able to ascertain independently the respective velocities of the isotropic and nematic phases at each position. Remarkably, we find that they can be different. As evidence for that assertion, we note our finding that the chosen value of ϕ could not simultaneously satisfy the state of both the isotropic peak and the nematic doublets. We are able to directly measure the phase at each peak and thus plot a separate velocity profile for the isotropic and nematic phases. These profiles will be shown in Fig. 12 and represent an important insight regarding the behavior of the CTAB system.

Figure 7 shows the relative proportions of the nematic phase obtained over a range of shear rates for the CTAB in D_2O system at 3 °C above the *I-N* transition. The open circles and squares show the optical and neutron-scattering results of Cappelaere *et al.*, while the closed circles are the equivalent proportions obtained in our NMR study. The agreement between the NMR and neutron-scattering data is quite remarkable.

B. NMR velocimetry

Figure 8 shows an example of displacement distributions obtained at a temperature of 40 °C and with an average gap shear rate of 105 s^{-1}. The deuteron NMR signals used to obtain these distributions arise from the water molecules of the solvent. The graph on the left shows displacement distributions that correspond to pixel positions, respectively, next to the inner (rotating) wall and the outer (stationary) wall. As expected, the outer wall distribution is a peak centered at zero, but with a finite width arising from the effect of water diffusion. The distribution seen at the inner wall has a peak position that is clearly shifted due to flow.

The position of the peak maximum is used in our software to obtain a velocity value for each corresponding pixel. Note, however, that the peak at the inner wall is distinctly skewed, reflecting significant contributions due to velocity values lower than the mode. Such skewed character is never seen in steady shear flow, for example in simple Newtonian liquids. Thus, while our velocity determination may return a ''mode'' value, inspection of these distributions invariably shows that over the course of the experiment of around 1 h, the velocity experienced within a particular image pixel has varied. This evidence strongly suggests that the flow field slowly fluctuates within the gap, with a characteristic time scale longer than the encoding time $\Delta = 50$ ms.

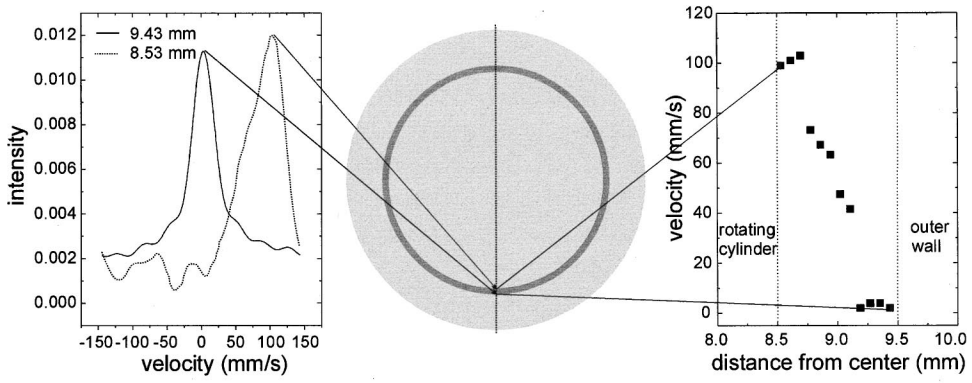

FIG. 8. NMR velocimetry analysis for a 20% w/v CTAB/D_2O sample at a temperature of 40 °C and with an average gap shear rate of 105 s^{-1}. The graph on the left shows displacement distributions for pixel positions, respectively, next to the inner (rotating) wall and the outer (stationary) wall. Note the broad distribution apparent at the inner wall, characteristic of velocity fluctuations over the acquisition time of more than 1 h. This skewed distribution indicates the existence of velocity values from zero to the wall maximum over this period. On the right is shown the profile of mode velocity values across the gap. Near the inner wall, the data lie on a line characteristic of near rigid body motion.

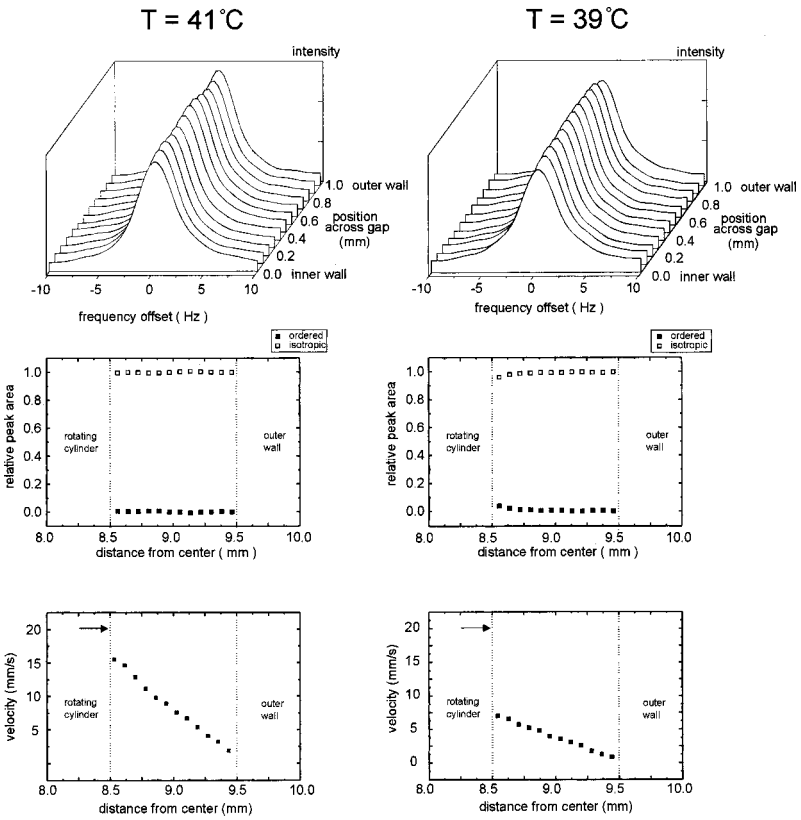

FIG. 9. A comparison of deuterium NMR spectra, order profiles and velocity profiles across the Couette cell gap, for a 20% w/v CTAB/D_2O sample with an average gap shear rate of 20 s^{-1} and at temperatures of 41 and 39 °C. Note that the isotropic phase prevails across the gap and that the mode velocity profiles show no evidence of shear banding. The arrows in the velocimetry data indicate the inner wall velocity. Slip is apparent in the 39 °C data set.

On the right-hand side of Fig. 8, we show the velocity profile across the gap as indicated by the peak mode displacements for the 39 °C CTAB/D_2O sample sheared at 105 s^{-1}. A number of remarkable features emerge in this particular experiment. First, we note that the fluid velocity at the inner wall is around 100 mm s^{-1}, identical to the wall value and thus indicating the lack of any slip under these particular conditions. Second, we note that over the first three pixels ($\sim$0.25 mm) out from the inner wall, the mode velocity *increases*, directly proportional to the radial displacement, and consistent with rigid body motion at nearly zero shear. Third, we note beyond that inner band a region of around 0.4-mm width, at which the velocity sharply declines and for which the average shear rate is around 300 s^{-1}. Finally, we observe an approximately 0.35-mm-wide region of practically zero shear near the outer wall. We will see when we compare this velocity profile with the corresponding deuterium spectra taken across the gap that the identification of a high-shear-rate phase with the nematic state is not at all obvious. These data indicate that the issue of shear banding in the CTAB/D_2O system is more complex than first thought.

C. Spectral and velocimetry comparisons

Figures 9, 10, and 11 present data obtained in experiments performed at different shear rates and different temperatures. In Fig. 9, we show mode velocity profiles and deuterium NMR spectra for temperatures of 41 and 39 °C and at a gap shear rate of 20 s^{-1}, right at the onset of the flow curve stress plateau. The data are quite straightforward. We see no clearly distinct split spectrum that we might identify with a nematic phase, although the width of the isotropic peak is larger than in the case of zero shear. In the bulk of the fluid, a uniform shear rate is experienced. However, in each case a significant slip is apparent at the inner wall.

Figure 10 shows the velocimetry and spectral data for a gap shear rate of 51 s^{-1} and at temperatures of 41, 40, and 39 °C. The chosen shear rate is positioned midplateau (see Fig. 3) and the temperatures are, respectively, 5, 4, and 3 °C above the equilibrium *I-N* transition. Note that in each case a nematic phase is apparent near the inner wall and that the extent of this phase increases as the temperature of the *I-N* transition is approached. In the velocimetry profiles, some slip at the inner wall is seen at 41 °C, but not at 40 or 39 °C. In each experiment performed at the three different temperatures, we see a low-shear-rate high-viscosity phase near the inner wall, followed by a high-shear-rate (300–400 s^{-1}) low-viscosity phase, and beyond that, a low-shear-rate high-viscosity phase completing the gap to the outer wall.

In each spectrum, it is possible to equate the high-viscosity low-shear-rate phase near the outer wall with an isotropic state. However, the nematic phase is not simply identified with the highly sheared state. Clearly, as one progresses across the gap towards the inner wall, the region of high shear corresponds to the region where significant nematic order starts to appear. However, in each experiment, the region near the inner wall corresponds to a highly nematic state but with low shear rate and high apparent viscosity. We do note, however, that in the pixel nearest the wall a slight enhancement of isotropic behavior is always indicated.

Figure 11 shows corresponding data obtained at 105 s^{-1}, near the end of the stress plateau. These experiments exhibited a growth in the extent of the nematic region as the tem-

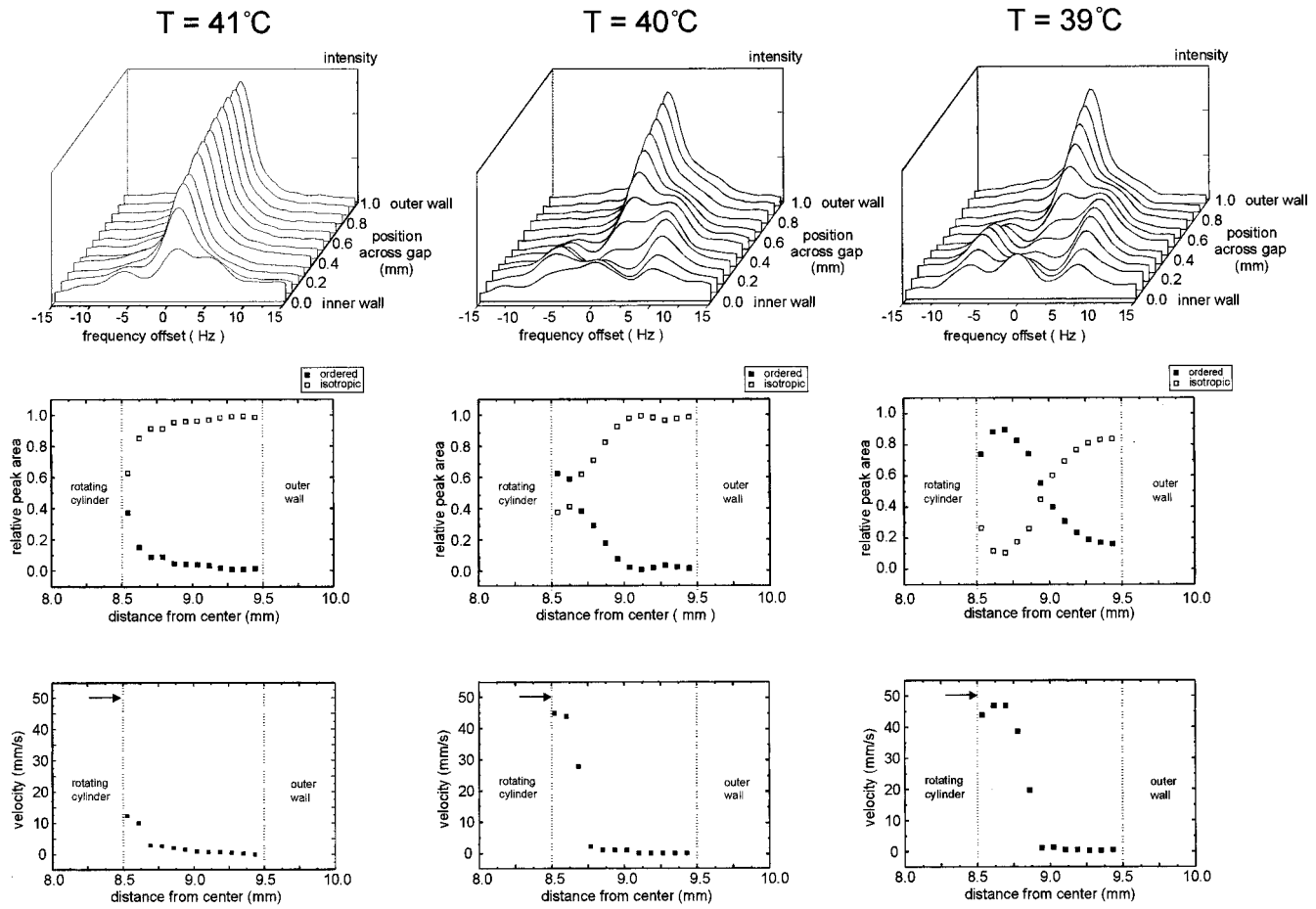

FIG. 10. A comparison of deuterium NMR spectra, order profiles, and velocity profiles across the Couette cell gap, for a 20% w/v CTAB/D_2O sample with an average gap shear rate of 51 s^{-1} and at temperatures of 41, 40, and 39 °C. Note that a transition from nematic to isotropic phases is evident in the profile from the inner to the outer wall. The velocimetry data indicate shear banding but it is clear that the nematic phase exists at low shear rate near the inner wall. Slip at the inner wall is apparent in the 39 °C data set.

perature is decreased, just as in the case of the 51 s^{-1} data set. However, unlike the 51 s^{-1} data set, no inner wall slip was observed, although at 41 and 40 °C, a similar progression from low shear rate to high shear rate to low shear rate was seen in the profile from the inner to the outer wall. The data at 39 °C are somewhat exceptional. Here a very high shear rate, tantamount to apparent slip, is seen at the outer wall, while across the gap the average shear rate appears to be on the order of 70 s^{-1}.

In order to make further sense of these velocity profiles, we show in Fig. 12 a comparison of the mode velocimetry data and the velocity profiles obtained separately for the isotropic and nematic peaks using the mean phase-shift method outlined earlier. We have chosen two representative cases. In the first, shown in Fig. 12(a), the gap shear rate is 20 s^{-1} and the temperature is 41 °C. Here the behavior is near-Newtonian. In the second case of 51 s^{-1} at a temperature of 39 °C, a significant isotropic-to-nematic ordering occurs along with notable shear banding. In the near-Newtonian case, the velocity profiles obtained by the two methods agree well. A so-called ''nematic'' profile is obtained by using the phase values obtained from the wings of the isotropic peak positioned at a frequency splitting of 15 Hz. The isotropic and nematic velocity profiles are consistent with each other.

In the case of 51 s^{-1} at a temperature of 39 °C [Fig. 12(b)], there is a significant discrepancy seen in the results obtained using the different methods. Note that velocimetry returns the mode whereas the phase-shift value returns the mean velocity distribution. A discrepancy between these methods is indicative of velocity fluctuations during the experiment. More importantly, we see that the mean isotropic velocity profile tends to lie below that of the mean nematic in the region of fluid near the inner wall, although the velocities are very similar at the inner wall itself. Such an observation could be consistent with the proposal that the small amount of isotropic fluid present in the region of the gap where the nematic component dominates tends to exist in a state of high shear. In contrast, the dominant nematic state exists at high viscosity with velocity values close to that of the inner wall.

DISCUSSION

In order to explain our results, we propose a model for shear-induced isotropic-to-nematic transitions, which inherently requires fluctuations in the flow field within the gap. This model is based on the idea that high shear banding drives the fluid nematic but that the state of nematic order so

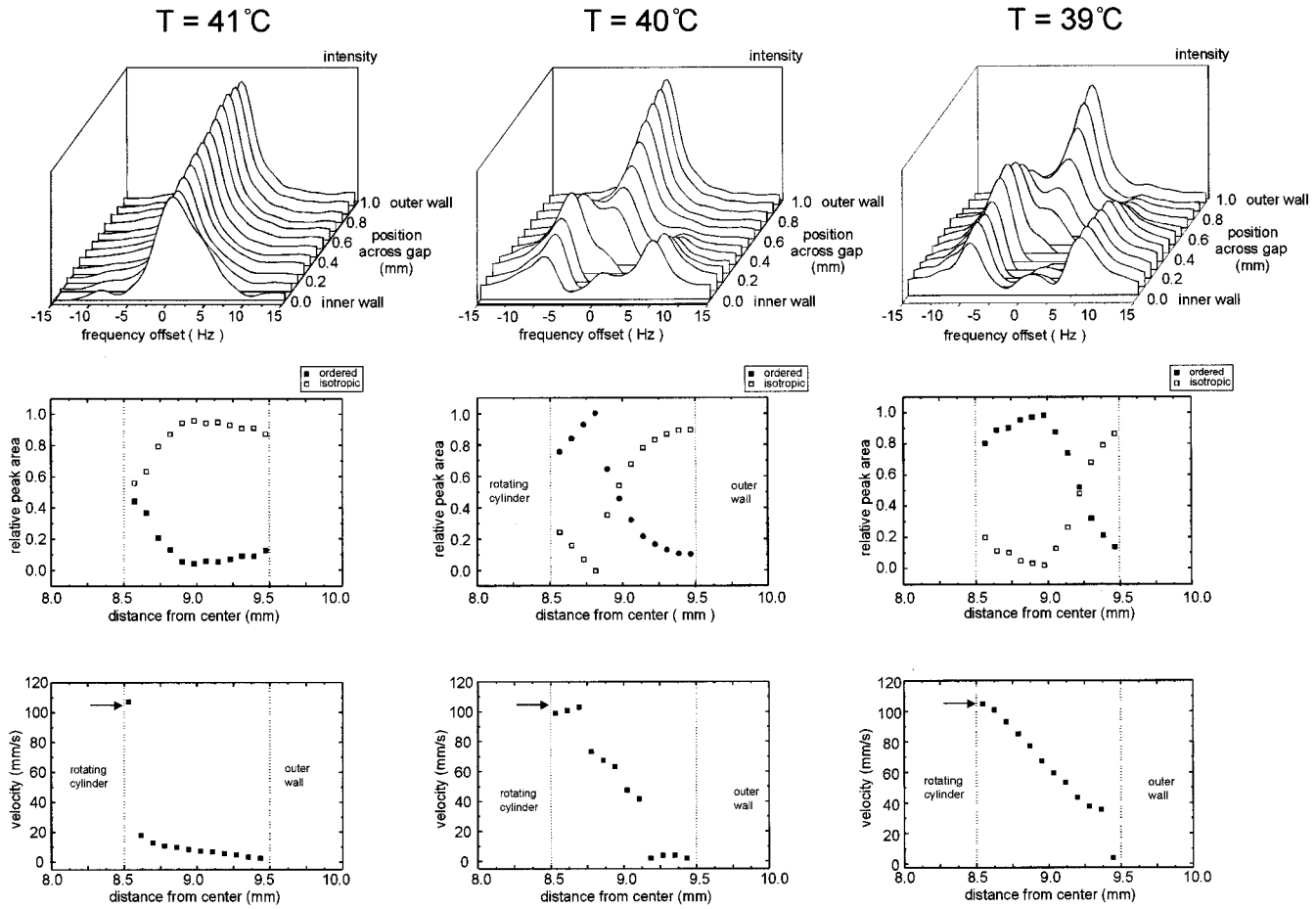

FIG. 11. As for Fig. 10 but with an average gap shear rate of 105 s^{-1}. Again, a transition from nematic to isotropic phases is evident in the profile from the inner to the outer wall. The mode velocity profiles are complex, but again there is no simple correspondence between a high shear rate band and the nematic phase. The data seen at 40 °C again clearly show that the nematic phase exists at low shear rate near the inner wall.

generated has high viscosity. Thus, a fluid element initially residing on the high-shear-rate branch of the flow curve reverts to a state of low shear once nematic order is induced. Further, we propose that once this low-shear-rate state is achieved, the nematic fluid element will, in time, relax back to its isotropic state, as would be expected in thermal equilibrium at zero shear. Figure 13(a) shows spectra following cessation of shear for fluid initially maintained at 105 s^{-1} at 39 °C, while Fig. 13(b) shows relaxation behavior of the nematic state. The relaxation process is multiexponential with the rapid time constant being on the order of or less than 1 s, and the longer one on the order of 20 s. It should be noted that these data were obtained after shearing the sample for many hours, the circumstances prevailing during a typical spatially resolved spectroscopy or velocimetry experiment. In contrast, when a fresh sample was sheared for only a few minutes, the amplitude of the rapid decay mode was dominant, with around 2% amplitude only, for the slow decay. We believe that these different behaviors point to the gradual buildup of mesoscale texture under shear. Clearly, the time scales for *N-I* relaxation will determine the rate of fluctuations that occur in the velocity field of the Couette cell gap.

We are thus able to model the fluid behavior as follows. First, we propose a schematic flow curve as shown in Fig. 14. This curve has separate isotropic and nematic branches, but we will assume that the high-shear-rate branch is a continuation of the stress plateau of the isotropic fluid, as might arise from an underlying constitutive instability of the Doi-Edwards type. *Unlike the simple rigid rod model, the high shear branch is not a state of nematic order*. Note that in a cylindrical Couette cell, under shear-rate controlled conditions, the absolute stress is indeterminate, but varies as the inverse squared radius. Thus the ratio of the inner to outer wall stresses is constant and the band of stress across the gap will superpose the (logarithmic) flow curve with a well-defined width, positioned according to the requirements that the fluid across the gap satisfy the mean shear rate. As shown in Fig. 14, such a stress band can be positioned with fluid in the high shear branch, but not necessarily at the highest stress within the gap. In other words, it is possible for the shear band to occur away from the inner wall. We will assume that fluid at higher stress than that experienced by the highly sheared layer is in the nematic state and on a high viscosity branch, as shown.

Second, we assume that the rate at which fluid is converted from an isotropic to a nematic state depends on the volume ϕ_2 of fluid contained at high shear, i.e., within the

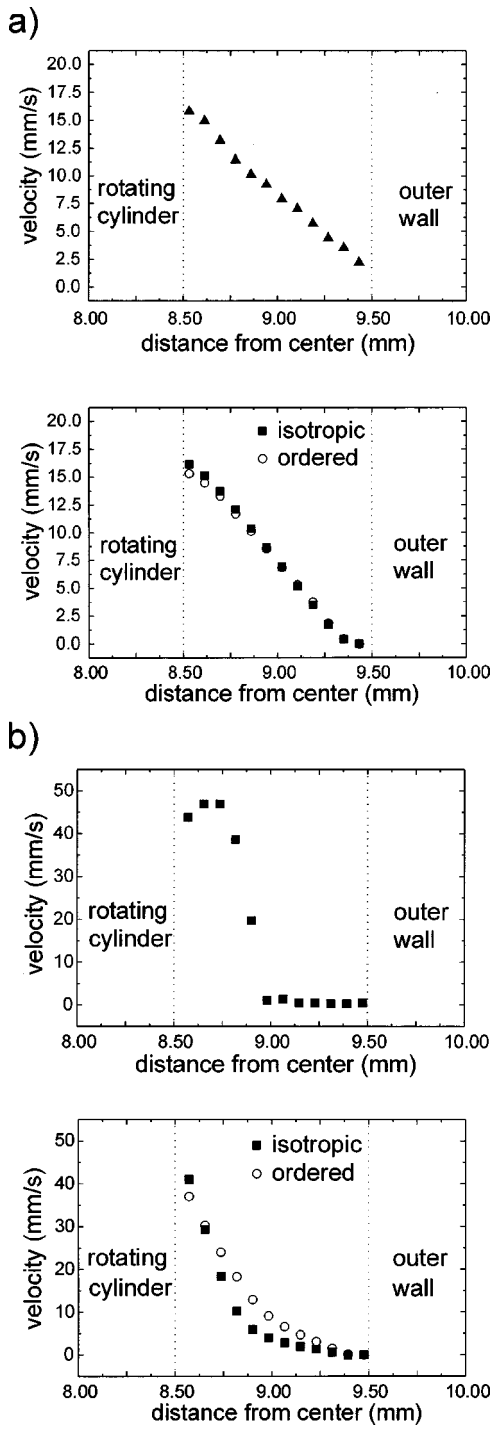

FIG. 12. Comparison of mode velocity profiles (upper graph) obtained from velocimetry and average velocity profile (lower graph) phases obtained by separately analyzing the phase shifts apparent on the spectroscopy data for the isotropic and nematic phases. (a) Near-Newtonian behavior is apparent at a gap shear rate of 20 s^{-1} and temperature 41 °C and the agreement between the two methods is excellent. (b) At a gap shear rate of 51 s^{-1} and temperature of 39 °C, shear banding behavior is apparent in the velocimetry (upper graph) while the mean phase shift data (lower graph) show a significant discrepancy. This lack of correspondence, along with the slight difference between the isotropic and ordered (nematic) profiles, is consistent with fluctuations in the order and velocity band structure.

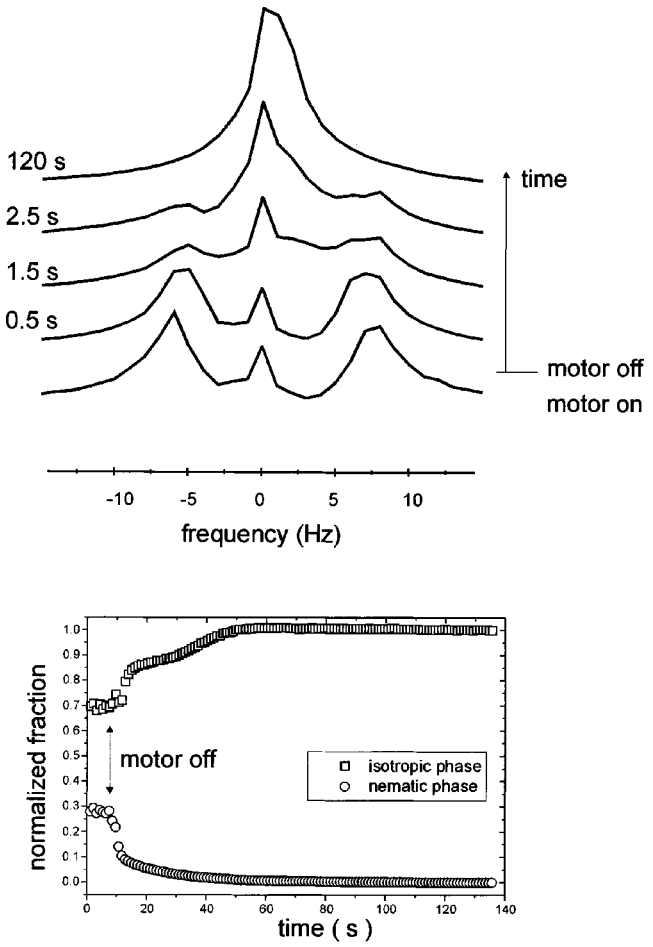

FIG. 13. Deuterium NMR spectra obtained during steady-state shear and subsequent to shear cessation for an initial gap shear rate of 105 s^{-1} and temperature 39 °C. The spectra after switch-off were obtained successively at 500 ms, 1.5, 2.5, and 120 s delay. (b) Time evolution of total nematic and isotropic fractions before and subsequent to cessation of shear. Note the multiple time constants apparent in the relaxation process.

highly sheared layer. Thus we set the conversion rate proportional to the deference between the gap shear rate and the low-shear-rate limit, $\dot{\gamma}_1$, of the stress plateau, i.e., proportional to $\dot{\gamma} - 15\,s^{-1}$. Third we assume that any fluid element, once driven nematic by residence in the high-shear-rate layer, will subsequently relax to an isotropic state with exponential probability and with a relaxation rate that depends upon temperature. Presumably this relaxation will be governed by the probability of forming an isotropic fluid element sufficiently large for nucleation and subsequent growth. Finally, we require that the flow field always readjusts such that the highly sheared layer (i.e., the fluid on the high shear branch) will jump to the isotropic fluid element of highest stress. Such a condition is consistent with the high shear branch being the highest possible stress state for any isotropic fluid element. The initial condition, where the fluid is entirely isotropic on startup of flow, is thus determined and requires that the highly sheared layer originate on the inner wall.

The simple model proposed above is easy to model nu-

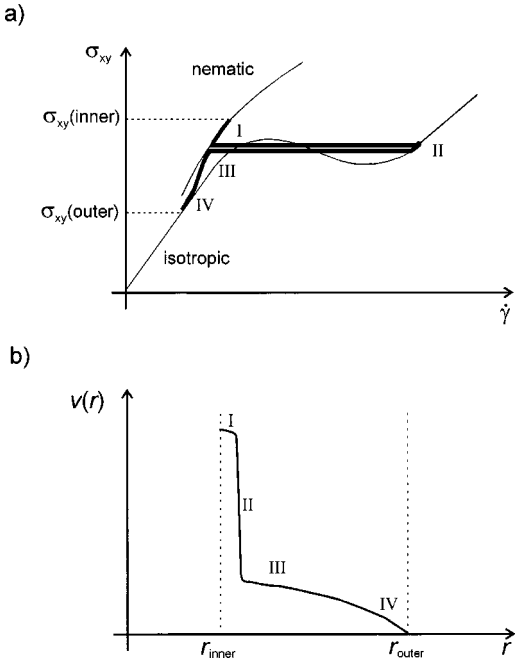

FIG. 14. Schematic constitutive flow curve consistent with the model proposed in this work in which a high viscosity (low shear rate) nematic branch exists. The schematic velocity profile associated with this curve is shown below.

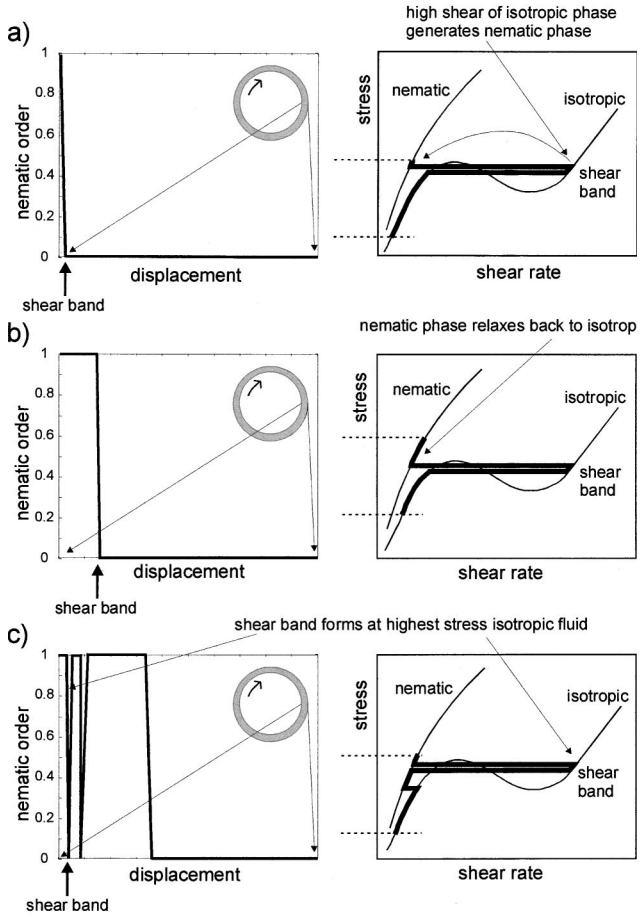

FIG. 15. Stress distributions and associated order profiles, at different points in the evolution of the band structure, according to the simple model based on a balance of *I-N* conversion and *N-I* relaxation. In (a), the high shear band generates a viscous nematic state and the stress readjusts to higher values. Subsequent relaxation (b) of nematic material generates in (c) a complex structure in which the shear band is positioned on the isotropic fluid at highest stress.

merically. A nematic, low-shear-rate phase begins to grow out from the inner wall bounded by a high-shear-rate layer of expanding radius, until a newly generated nematic fluid element, inside that layer, is able to relax back to an isotropic state. As soon as that happens, the high shear layer jumps back in radius to this new position. Relaxation from nematic to isotropic states may occur without jumps in the position of the high shear layer, provided that these transitions occur at lower stress than that experienced by the currently selected high shear layer. Relaxation of an element at higher stress will, however, always result in a repositioning of the layer to lower radius. Thus a competitive process is established in which the averaged degree of nematic order will vary across the gap, the extent of the nematic band penetration depending on shear rate (*I-N* transition rate) and temperature (*N-I* relaxation). In this competition, the highly sheared layer wanders about with a characteristic time on the order of many seconds. For low temperatures and high shear rates, the highly sheared layer may seldom approach the inner wall very closely but be mostly positioned midgap. Nonetheless, the velocity distribution of an inner layer will be skewed from the mode (the wall speed) down to low velocities, corresponding to periods when high shearing occurs locally. This is exactly what is observed in Fig. 8. Furthermore, whenever the fluid is locally isotropic, it will be either highly sheared or at low (outer band) velocities, whereas in a nematic state the fluid is capable of experiencing high (inner band) velocities due to being in a viscous state close to the inner wall. As a consequence, we expect that mean nematic velocities will exceed mean isotropic velocities, exactly as seen in Fig. 12.

In the numerical modeling, the gap is divided into 100 spatial elements and the rate of *I-N* conversion in each element is set to two elemental volumes per time step in the case of the highest shear rate (105 s^{-1}). The *N-I* relaxation time constant, τ, per nematic element is set to 1000 time steps at 40 °C and varied with temperature so as to fit the data [see Fig. 16(b)]. In modeling the relaxation process, the function $\exp(-(t-t')/\tau)$ is compared with a random number between 0 and 1 to determine whether a decay to the isotropic state occurs, where t is the current time and t' is the time at which the nematic state was created. Figure 15 shows a set of representative instantaneous order-parameter profiles calculated using this simple model. Note the fluctuation in the position of the highly sheared band in accordance with the description above. Figure 16 shows the result of a time-averaged sequence in which the degree of order is averaged over 10 000 time steps. For this number of steps, a well-defined steady-state distribution is apparent. Superposed on the calculated profiles in Fig. 16(a) are the observed order-parameter distributions for the 20, 51, and 105 s^{-1} experiments, at a temperature of 39 °C. For these data, the relax-

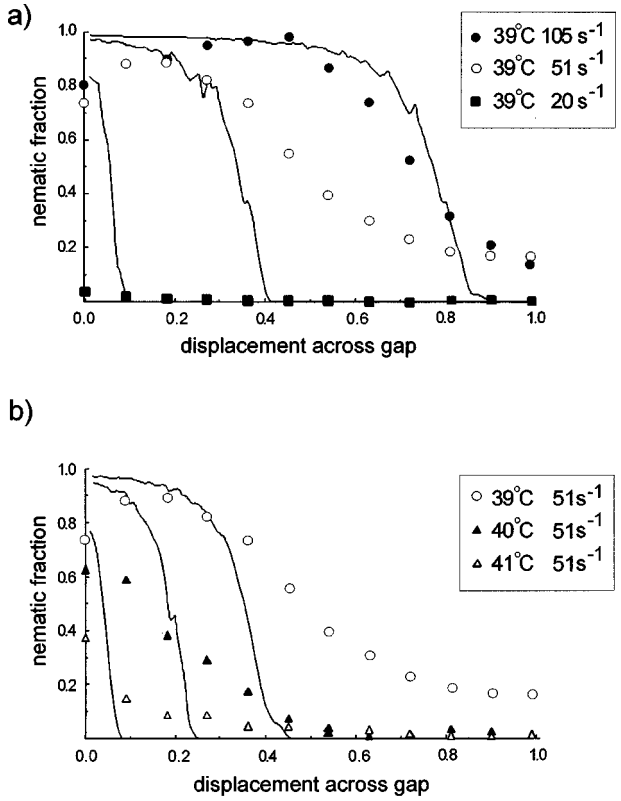

FIG. 16. Mean order profiles, calculated using the simple model of Fig. 15, averaged over a sufficient number of time steps to generate an asymptotic result. (a) shows the comparison of the data obtained at fixed temperature along with the theoretical curves, in which the conversion rate is set proportional to the displacement of the shear from the onset of the plateau. (b) shows the comparison of the data obtained at fixed shear rate along with the theoretical curves, in which the relaxation rate scales as $\sim \Delta T^6$.

ation time constant is fixed at 3500 time units and the *I-N* transition rate is scaled as $\dot{\gamma} - 15\,\mathrm{s}^{-1}$. Figure 16(b) shows the variation with temperature at a fixed shear rate of 51 s^{-1}. The respective relaxation times used to represent the data at 39, 40, and 41 °C are 3500, 1000, and 50 time steps. The numerical parameters used for the time series shown in Fig. 15 correspond to the case of 105 s^{-1} and 40 °C and were chosen to give a reasonable fit. Thus the *N-I* relaxation rate appears to scale quite steeply as ΔT^{α}, where ΔT is the temperature difference from the equilibrium isotropic transition and $\alpha = 6$.

CONCLUSION

By means of deuterium NMR spectroscopy on the heavy water molecule probe, we are able to observe nematic ordering in the system CTAB/D_2O. The splittings observed in the nematic phase are independent of shear rate and consistent with the formation of a highly ordered micellar state. The small size of the splitting, of around 15 Hz, results from motionally averaged sampling of the structure by the water molecule, in which the residual order inherited by the deuteron order is around 10^{-5}. We show that the width of the nematic region in the annular gap of our Couette cell depends on shear rate. Our results are consistent with the observation in birefringence studies of a bright h-band whose width depends on shear rate, and in exact quantitative agreement with the degree of order measured in neutron-diffraction measurements. We also show that the nematic bandwidth depends strongly on proximity to the equilibrium *I-N* transition. Our measurements of the dependence of a nematic fraction on shear rate agree well with independent neutron-scattering data on the same system.

We are able to use NMR velocimetry to measure velocity profiles under the same shear rate and temperature conditions used in the spectroscopic study, observing both wall slip and shear banding effects. Close analysis of the velocity distribution in individual pixels suggests that the velocity field exhibits fluctuations, a conclusion supported by comparison of mean and mode values. Our results clearly indicate that shear banding and nematic ordering effects are related but that the induced nematic state is certainly not a state of high shear rate and low viscosity. On the contrary, we observe exceedingly low shear rates in clearly nematic fluid under conditions of high stress existing near the wall of the inner cylinder, and this leads us to conclude that the process of shearing induces a nematic state of high viscosity. We conjecture that the viscous nature of this phase is connected with mesoscale ordering, a proposition supported by our observations of relaxation following shear cessation after different periods of buildup. This mesoscale behavior may arise from micellar association, aided by alignment, or by the formation of higher-order texture. One might ask why such high viscosity behavior is not seen in mechanical rheometry studies on the nematic phase. It may be that the shear-induced nematic phase differs from that formed in equilibrium. Alternatively, mechanical rheometry may be confounded by slip effects. We note that in velocimetry experiments performed here on the thermal equilibrium nematic phase, a high degree of slip was observed.

Because of the viscous nature of the nematic state generated under shear, no steady-state banded structure is possible, since the high shear band in due course evolves to a low sheared phase. The continuous transitions from the high shear branch to the viscous nematic branch are counterbalanced by subsequent relaxation of nematic order. A simple model based on this competition provides a nice representation of our order profiles, along with their dependence on shear rate and temperature. It also accounts for the apparent fluctuations in velocity profiles suggested by the broad velocity distributions measured in each pixel.

Our work raises a number of intriguing questions. What is the characteristic time scale for any fluctuations in the velocity field, and do these times correspond with the measured time constants for relaxation from the nematic to isotropic state on cessation of shear? In our experiments, we find that the magnitude of the isotropic component is always perceptibly larger at the inner wall. Does the wall inhibit ordering or does this increased isotropic behavior reflect a predominant positioning of the highly shear layer at the rotating surface? We suggest that time-resolved velocimetry and birefringence measurements at high spatial resolution will be

needed to elucidate these issues.

The most pressing question raised by our work concerns the nature of the shear-induced nematic phase. Why is the nematic state in wormlike micelles highly viscous, in contrast with the lowered viscosity state expected for rigid rods? In this context, we note with interest the finding of Pines and co-workers [57] that certain micellar systems may form gel states when ordered under shear. We propose that the shear-induced nematic state of CTAB/D_2O exhibits a mesophase structure consistent with enhanced viscosity.

It is clear that shear banding and order banding do not necessarily coincide. The use of velocimetry profiling is therefore strongly indicated in any experiments in which ordering effects are examined via scattering, birefringence, or NMR spectroscopy experiments. The data presented here indicate the value of measuring both shear rate and order profiles under the same conditions. Failure to do so can lead to misinterpretation of the hydrodynamic state of highly ordered fluid. While the present NMR work reveals a degree of complexity in the behavior of wormlike micelles that was hitherto unsuspected, the outcome of this work is also helpful in bridging the gap between the various spectroscopic methods. In particular, we believe that the correspondence of birefringence effects and quadrupolar splitting effects in the CTAB/D_2O system, along with the close quantitative agreement found between NMR and neutron-scattering measurements of nematic fractions, helps in providing a useful link between optical, neutron-scattering, and NMR investigations.

We would caution that the observations contained in this study are peculiar to the particular system being investigated, namely a non-Maxwellian wormlike micellar system in the concentrated regime, and close to an *I-N* transition. Nonetheless, we suggest that the results have significant implications for the modeling of flow instabilities in nematic systems.

ACKNOWLEDGMENTS

E.F. wishes to thank the Deutsche Forschungsgemeinschaft for Financial support. Financial support from the Royal Society of New Zealand Marsden Fund is also gratefully acknowledged.

[1] G. V. Vinogradov, Rheol. Acta **12**, 357 (1973).
[2] M. Doi and S. F. Edwards, J. Chem. Soc., Faraday Trans. **74**, 1789 (1978).
[3] M. Doi and S. F. Edwards, *The Theory of Polymer Dynamics* (Oxford University Press, Oxford, 1987).
[4] T. C. B. Mcleish and R. C. Ball, J. Polym. Sci., Polym. Phys. Ed. **24**, 1735 (1986).
[5] M. E. Cates, T. C. B. Mcleish, and G. Marrucci, Europhys. Lett. **21**, 451 (1993).
[6] R. Rehage and H. Hoffmann, Mol. Phys. **74**, 933 (1991).
[7] A. Khatory, F. Lequeux, F. Kern, and S. J. Candau, Langmuir **9**, 1456 (1993).
[8] T. M. Clausen, P. K. Vinson, J. R. Minter, H. T. Davis, Y. Talmon, and W. G. Miller, J. Phys. Chem. **96**, 474 (1992).
[9] S. J. Candau, E. Hirsch, and R. Zana, J. Colloid Interface Sci. **105**, 521 (1985).
[10] G. Porte, J. Appel, and Y. Poggi, J. Phys. Chem. **84**, 3105 (1980).
[11] M. E. Cates, J. Phys. Chem. **94**, 371 (1990).
[12] J.-F. Berret, D. Roux, G. Porte, and P. Lindner, Europhys. Lett. **25**, 521 (1994).
[13] O. El Haitamy, Thése de troisieme cycle, Université de Montpelier, France, 1985 (unpublished).
[14] E. Cappelaere, R. Cressely, and J. P. Decruppe, Colloids Surf., A **104**, 355 (1995).
[15] A. Onuki and K. Kawasaki, Ann. Phys. **121**, 456 (1979).
[16] E. Helfand and G. H. Fredrickson, Phys. Rev. Lett. **62**, 2468 (1989).
[17] G. H. Fredrickson and R. G. Larson, J. Chem. Phys. **86**, 1553 (1987).
[18] M. E. Cates and S. T. Milner, Phys. Rev. Lett. **62**, 1856 (1989).
[19] P. D. Olmsted and P. Goldbart, Phys. Rev. A **41**, 4578 (1990).
[20] P. D. Olmsted and P. Goldbart, Mol. Cryst. Liq. Cryst. **198**, 265 (1991).
[21] H. See, M. Doi, and R. G. Larson, J. Chem. Phys. **92**, 792 (1990).
[22] P. D. Olmsted and P. Goldbart, Phys. Rev. A **46**, 4966 (1992).
[23] G. Porte, J.-F. Berret, and J. L. Harden, J. Phys. II **7**, 459 (1997).
[24] E. Cappelaere, J.-F. Berret, J. P. Decruppe, R. Cressely, and P. Lindner, Phys. Rev. E **56**, 1869 (1997).
[25] D. C. Roux, J.-F. Berret, G. Porte, E. Peuvrel-Disdier, and P. Lindner, Macromolecules **28**, 1681 (1995).
[26] V. Schmidt, F. Lequeux, A. Pousse, and D. Roux, Langmuir **10**, 955 (1994).
[27] M. S. Turner and M. E. Cates, Langmuir 1590 (1991).
[28] N. A. Spenley, M. E. Cates, and T. C. B. McLeish, Phys. Rev. Lett. **71**, 939 (1993).
[29] N. A. Spenley, X. F. Yuan, and M. E. Cates, J. Phys. II **6**, 551 (1996).
[30] P. D. Olmsted and C.-Y. D. Lu, Phys. Rev. E **60**, 4397 (1999).
[31] P. D. Olmsted, Europhys. Lett. **48**, 339 (1999).
[32] O. Radulescu, P. D. Olmsted, and C. Y. D. Lu, Rheol. Acta **38**, 13 (1999).
[33] J.-F. Berret, D. C. Roux, and G. Porte, J. Phys. II **4**, 1261 (1994).
[34] J. P. Decruppe, R. Cressely, R. Makhloufi, and E. Cappelaere, Colloid Polym. Sci. **273**, 346 (1995).
[35] R. Makhloufi, J. P. Decruppe, A. Ait-Ali, and R. Cressely, Europhys. Lett. **32**, 253 (1995).
[36] J.-F. Berret and D. C. Roux, J. Rheol. **39**, 725 (1995).
[37] J.-F. Berret, G. Porte, and J. P. Decruppe, Phys. Rev. E **55**, 1668 (1997).
[38] J. P. Decruppe, E. Cappelare, and R. Cressely, J. Phys. II **7**, 257 (1997).
[39] P. Fischer, Rheol. Acta **39**, 234 (2000).
[40] P. T. Callaghan, M. E. Cates, C. J. Rofe, and J. B. A. F. Smeulders, J. Phys. II **6**, 375 (1996).

[41] R. W. Mair and P. T. Callaghan, Europhys. Lett. **36**, 719 (1996).
[42] R. W. Mair and P. T. Callaghan, J. Rheol. **41**, 901 (1997).
[43] M. M. Britton and P. T. Callaghan, Phys. Rev. Lett. **78**, 4930 (1997).
[44] M. M. Britton and P. T. Callaghan, Eur. Phys. J. B **7**, 237 (1999).
[45] M. M. Britton, R. W. Mair, R. K. Lambert, and P. T. Callaghan, J. Rheol. **43**, 897 (1999).
[46] E. Fischer and P. T. Callaghan, Europhys. Lett. **50**, 803 (2000).
[47] M. E. Cates, Macromolecules **20**, 2289 (1987).
[48] C. Rangel-Nafaile, A. B. Metzner, and K. F. Wissbrun, Macromolecules **17**, 1187 (1984).
[49] S. T. Milner, Phys. Rev. Lett. **66**, 1477 (1991).
[50] O. Radulescu and P. D. Olmsted, J. Non-Newtonian Fluid Mech. **91**, 143 (2000).
[51] P. D. Olmsted, O. Radulescu, and C. Y. D. Lu, J. Rheol. **44**, 257 (2000).
[52] C. Y. D. Lu, P. D. Olmsted, and R. C. Ball, Phys. Rev. Lett. **84**, 642 (2000).
[53] A. Abragam, *Principles of Nuclear Magnetism* (Oxford University Press, Oxford, 1963).
[54] P. T. Callaghan, *Principles of Nuclear Magnetic Resonance Microscopy* (Oxford University Press, Oxford, 1991).
[55] B. Deloche and E. T. Samulski, Macromolecules **14**, 575 (1981).
[56] M. M. Britton, P. T. Callaghan, M. L. Kilfoil, R. W. Mair, and K. Owens, Appl. Magn. Reson. **15**, 287 (1998).
[57] S. L. Keller, P. Boltenhagen, D. J. Pine, and J. A. Zasadzinski, Phys. Rev. Lett. **80**, 2725 (1998).